

This is a self-archived version of an original article. This version may differ from the original in pagination and typographic details.

Author(s): Maurel, Alexis; Haukka, Matti; MacDonald, Eric; Kivijärvi, Lauri; Lahtinen, Elmeri; Kim, Hyeonseok; Armand, Michel; Cayla, Aurélie; Jamali, Arash; Grugeon, Sylvie; Dupont, Loic; Panier, Stéphane

Title: Considering lithium-ion battery 3D-printing via thermoplastic material extrusion and polymer powder bed fusion

Year: 2021

Version: Accepted version (Final draft)

Copyright: © 2020 Elsevier B.V. All rights reserved.

Rights: CC BY-NC-ND 4.0

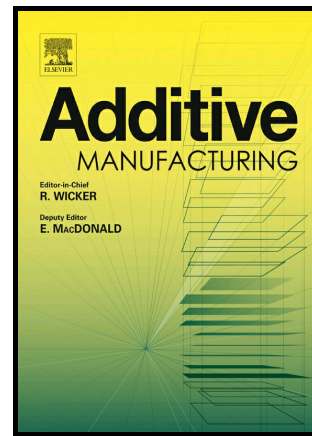
Rights url: <https://creativecommons.org/licenses/by-nc-nd/4.0/>

Please cite the original version:

Maurel, A., Haukka, M., MacDonald, E., Kivijärvi, L., Lahtinen, E., Kim, H., Armand, M., Cayla, A., Jamali, A., Grugeon, S., Dupont, L., & Panier, S. (2021). Considering lithium-ion battery 3D-printing via thermoplastic material extrusion and polymer powder bed fusion. *Additive Manufacturing*, 37, Article 101651. <https://doi.org/10.1016/j.addma.2020.101651>

Considering Lithium-ion Battery 3D-printing via Thermoplastic Material Extrusion and Polymer Powder Bed Fusion

Alexis Maurel, Matti Haukka, Eric MacDonald, Lauri Kivijärvi, Elmeri Lahtinen, Hyeonseok Kim, Michel Armand, Aurélie Cayla, Arash Jamali, Sylvie Grugeon, Loic Dupont, Stéphane Panier



PII: S2214-8604(20)31023-X

DOI: <https://doi.org/10.1016/j.addma.2020.101651>

Reference: ADDMA101651

To appear in: *Additive Manufacturing*

Received date: 16 July 2020

Revised date: 5 October 2020

Accepted date: 5 October 2020

Please cite this article as: Alexis Maurel, Matti Haukka, Eric MacDonald, Lauri Kivijärvi, Elmeri Lahtinen, Hyeonseok Kim, Michel Armand, Aurélie Cayla, Arash Jamali, Sylvie Grugeon, Loic Dupont and Stéphane Panier, Considering Lithium-ion Battery 3D-printing via Thermoplastic Material Extrusion and Polymer Powder Bed Fusion, *Additive Manufacturing*, (2020) doi:<https://doi.org/10.1016/j.addma.2020.101651>

This is a PDF file of an article that has undergone enhancements after acceptance, such as the addition of a cover page and metadata, and formatting for readability, but it is not yet the definitive version of record. This version will undergo additional copyediting, typesetting and review before it is published in its final form, but we are providing this version to give early visibility of the article. Please note that, during the production process, errors may be discovered which could affect the content, and all legal disclaimers that apply to the journal pertain.

Considering Lithium-ion Battery 3D-printing via Thermoplastic Material Extrusion and Polymer Powder Bed Fusion

Alexis Maurel^{a,b,c,*}, Matti Haukka^d, Eric MacDonald^e, Lauri Kivijärvi^d, Elmeri Lahtinen^d, Hyeonseok Kim^{a,c}, Michel Armand^a, Aurélie Cayla^{f,g}, Arash Jamali^h, Sylvie Grugeon^{a,c}, Loic Dupont^{a,c,h,*} & Stéphane Panier^{b*}

^a Laboratoire de Réactivité et de Chimie des Solides, UMR CNRS 7314, Hub de l'Énergie, Université de Picardie Jules Verne, 33 rue Saint Leu, 80039, Amiens Cedex, France

^b Laboratoire des Technologies Innovantes, LTI-EA 3899, Université de Picardie Jules Verne, 80025 Amiens, France

^c RS2E, Réseau français sur le stockage électrochimique de l'énergie, FR CNRS 3459, 80039 Amiens Cedex, France

^d Department of Chemistry, P.O. Box 35, Street Address: Survantie 9 B, FI-40014 University of Jyväskylä, Finland

^e Electrical & Computer Engineering, Youngstown State University, Youngstown, OH, USA

^f Université Lille Nord de France, F-59000 Lille, France

^g ENSAIT, GEMTEX, F-59100 Roubaix, France

^h Plateforme de Microscopie Électronique (PME) de l'Université de Picardie Jules Verne, Hub de l'Énergie, 15 rue Baudelocque, 80000 Amiens, France

* alexis.maurel@u-picardie.fr

* loic.dupont@u-picardie.fr

* stephane.panier@u-picardie.fr

ABSTRACT

In this paper, the ability to 3D print lithium-ion batteries through thermoplastic material extrusion and polymer powder bed fusion is considered. Focused on the formulation of positive electrodes composed of polypropylene, LiFePO₄ as active material, and conductive additives, advantages and drawbacks of both additive manufacturing technologies, are thoroughly discussed from the electrochemical, electrical, morphological and mechanical perspectives. Based on these preliminary results, strategies to further optimize the electrochemical performances are proposed. Through a comprehensive modeling study, the enhanced electrochemical suitability at high current densities of various complex three-dimensional lithium-ion battery architectures, in comparison with classical two-dimensional planar design, is highlighted. Finally, the direct printing capability of the complete lithium-ion battery by means of multi-materials printing options processes is examined.

Keywords: Lithium-ion battery, Electrodes, Material extrusion, Powder bed fusion, Composites.

1. Introduction

Electrochemical energy storage is a crucial subsystem required to enable the 3D printing of next generation products including geometrically-complex and mass-customized smart structures [1-6]. Embedding electronics, sensors, antennas and batteries into arbitrary shapes is the next inevitable advancement in the evolution of additive manufacturing (AM) (Figure 1), which can be interrupted to leverage complementary manufacturing processes. Printers will fabricate products with more than mechanical capability, but rather will now include electronic, optical, chemical, biological, thermal, and electromagnetic functions. In this context, multi-process (or hybrid) 3D printing provides the simultaneous benefits of 3D printing - complex and customized geometries - with those known advantages of traditional processes - tight dimensional accuracies and superior surface finish from machining, cutting, dispensing, and robotic component placement. However, one conspicuously-absent functionality in this hybrid manufacturing paradigm has been energy storage: either directly printed batteries as pursued in this seminal research effort and our previous works [7-10], or even the simple insertion of non-printed electronic components such as traditional batteries into cavities in 3D printed structures [1, 11]. Due to the high temperatures required for printing, a commercial lithium ion battery (LIB) component that is introduced into a predefined cavity, can be damaged upon pursuing the printing process. A detrimental effect on the resulting electrochemical performances and

safety of the device is thus expected, as liquid electrolyte (solvent-based) will evaporate, leading to a high internal pressure within the battery casing itself. In order to overcome these particular issues, the direct printability of the complete LIB where the liquid electrolyte must be infused within the electrodes at room temperature (once printing is finished), appears as a promising solution. By interweaving energy storage within a complex and multi-functional 3D structure, new levels of both spatial and energy efficiency will now be possible. The 3D printing of high energy density storage is paramount for the wider adoption of hybrid AM to create structural electronics, smart implants, and next-generation aerospace products.

AM technologies have recently been explored with a view to manufacture energy storage devices such as LIB employing a layer-upon-layer material deposition methodology [12-19]. This approach offers the possibility of obtaining complex three-dimensional electrodes unlike the conventional fabrication techniques such as doctor-blading or die-pressing. As reported in literature [20-24], 3D electrode designs result theoretically in enhanced electrochemical performance in terms of specific capacity and power due to the increased active surface area and theoretical lithium cations diffusion in three dimensions. Fabricating 3D electrodes was attempted by performing an electrochemical growth of nanorods onto a current collector followed by electrochemical plating of the active material[25]. Nonetheless, the resulting structure often presented surface irregularities resulting in short-circuits even prior to cycling. These issues can be overcome by leveraging AM processes, enabling the interpenetration of complex positive and negative electrode lattice structures. So far, by means of AM, studies are rather focused on achievable short-term objectives: implementing a topological optimization of the energy storage by reducing dead-volume and dead-weight within the final object [8, 23, 26, 27]. Among the AM processes, thermoplastic material extrusion (ME) and polymer powder bed fusion (PBF) are considered as two promising options to print LIB electrodes with a diversity of shapes as depicted hereafter.

A ME printer is classically fed with a thermoplastic filament constituted of polylactic acid (PLA), polyethylene terephthalate glycol (PETG), acrylonitrile-butadiene-styrene, polycarbonate, or also polypropylene (PP), among other engineering grade polymers. The filament is driven through a computer-controlled heated nozzle, extruded on to the substrate, and immediately solidifies. The molten material is thus deposited layer after layer with the aim to obtain the desired 3D object [15, 18, 28, 29]. Besides the development of 3D printing technology and composite filaments, 3D printing of LIB has witnessed rapid advancements. This tendency is mainly due to the ability of 3D printing to create LIB components that do not require further post-processing and also motivated by the printability of the complete energy storage device in one single, non-assembly process. Nonetheless, it must be emphasized that a sufficient quantity of charges (active material and conductive additives) is required within the electrodes with an objective of achieving reasonable electrochemical performances. This requirement, coupled with the filament-shape constraint, renders the formulation process rather complex. Hence, printing of various commercial or homemade composite filaments containing a limited amount of LIB active materials (only between 8 and 13 wt% of the total electrode) have been reported, resulting in mediocre electrochemical performances [26, 30]. Alternatively, the present effort has focused on the authors' previous studies [7, 8] aimed at increasing the active material loading within the filament to maximize the electrochemical performances while simultaneously maintaining sufficient mechanical properties. Indeed, a significant landmark was reached as active material loading was increased up to 49 wt% within 3D-printable PLA/LiFePO₄ and PLA/graphite filaments [7, 8]. These highly loaded filaments were achieved thanks to the introduction of a plasticizer such as poly(ethylene glycol) dimethyl ether (average Mn 500) which improves the printability. Logically, the improved filament resulted in higher electrochemical performances [10]: 200 mAh g⁻¹ of active material (99 mAh g⁻¹ of the total composite or also to 154.6 mAh cm⁻³) at current density of 18.6 mA g⁻¹ (C/20) for the PLA/graphite 3D-printed negative electrode disc [7]; 87 mAh g⁻¹ of active material (43 mAh g⁻¹ of the total composite or also up to 66 mAh cm⁻³) at current density of 8.5 mA g⁻¹ (C/20) for the PLA/LiFePO₄ 3D-printed positive electrode disc [8]. Finally, it is worth mentioning that extrusion and the associated printing parameters (e.g. temperature) generally require tedious and comprehensive adjustments to match the LIB-specific expectations.

As an alternative to the ME printing, polymer PBF involves the spreading and leveling of a consistent and thin layer of powder with a blade upon the building platform. Then, a high energy CO₂ LASER (14 Watt) is applied selectively (computer-controlled) to fuse together small powder particles (typical diameter of 50–100 μm). After each layer is completed, the platform is subsequently lowered and a new layer of powder is dispensed. This process is repeated layer by layer until the final 3D object is built. Usually, the final 3D printed item requires post processing to remove unfused powder excess. Physical characteristics such as the porosity and mechanical strength can be controlled by

fine-tuning the printing parameters such as the laser power, exposure time, and printing temperature. The most significant advantage of PBF when compared to ME is the ability to add charges (active material and conductive additives) into the printed object by simply mixing it with the polymer powder prior to selectively melting (no filament required). Typical printing polymer materials include polyamides (PA), PP, polystyrene (PS) and polyurethane (PU). Consequently, many studies have reported the introduction of fillers within the polymer matrix to print objects with improved properties for particular applications. PA-based composite powder (PA11/carbon-nanofibers, PA12/multi-walled-carbon-nanotubes, PA11/carbon-nanotubes, PA11/nanographene platelets, PA11/SiO₂, PA11/Al₂O₃, PA12/carbon-black and PA11/montmorillonite) with enhanced flame retardancy, electrical conductivity, thermal, and mechanical properties for PBF have been developed [31-36]. By sintering the polymer particles in such a way that only their surfaces are partially melted, highly porous objects can be obtained, thus the modified process is well suited for printing LIB electrodes. Indeed, when the polymer particles are only partially sintered, the charges are thus distributed on the surface of these particles and are therefore accessible by liquids such as the electrolyte flowing through the printed electrode [37, 38]. In our previous study [39], PBF was employed to fabricate highly porous carbonaceous PA12/graphite, PS/graphite and PU/graphite electrodes that could be used in LIB applications. A relatively low amount of charge (active material) was introduced with a view to achieve highly porous electrodes with suitable mechanical strength. As one can expect, the graphite concentration, polymer matrix, and printing conditions all had an impact on the final mechanical strength, porosity, conductivity, and thus future electrochemical performances. In order to reach foam structure of electrochemically-active materials by means of PBF, an additional post-process step was proposed by Sha et al. [40]. The authors proposed a template method to print 3D graphene foams from of a homogeneous Ni/sucrose powder mixture, followed by Ni etching as post-processing step. Sucrose was used as the carbon source after calcination during printing while Ni served as the catalyst and template for graphene growth. Regarding the PBF technique, it is worth-mentioning that, up to our knowledge, no paper on literature reported so far electrochemical performances of independently printed LIB electrodes.

In the present study, the ability to 3D print LIB through two particularly different AM processes, ME and PBF, is considered. The working process, requirements for printing materials in each case, resolution, advantages and drawbacks of each technique to print electrodes are discussed. Perspectives towards their future optimization are proposed on the basis of experimental results of a comparative study specifically focused on the formulation of a positive electrode composed of PP acting as polymer matrix, LiFePO₄ (LFP) as active material, and carbon black (C45) as conductive additives. As a preliminary study, the extrusion (ME) and printing parameters (ME and PBF) were kept unchanged while for each printing techniques, the same electrochemically-active material loading was first tested and then increased as high as possible. Finally, the electrochemical suitability of various three-dimensional LIB architectures, in comparison with classical two-dimensional planar design, is thoroughly studied through an in-depth modeling study, and the direct printing capability of the complete LIB by means of both processes is examined. In this work, for the first time, electrochemical characterization of LIB electrodes printed via PBF is reported.

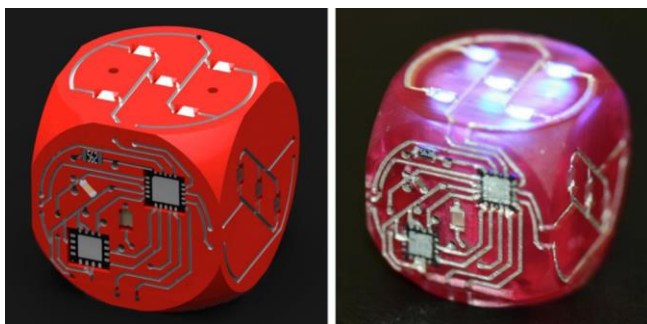


Figure 1. 3D printed gaming die with embedded microcontroller and accelerometer [11]. A battery was inserted into the structure after fabrication and curing, however the proposed effort could allow for more spatially-efficient and seamless integration of energy storage.

2. Experimental methodology

2.1. Materials

For both processes, the same materials were employed. Polypropylene powder AdSint® PP flex (particle size: 70 μm) was provided by Advanc3d Materials, Germany. Aleees (Taiwan) LiFePO_4 (LFP) (particle size: 1 μm) was used as active material for the positive electrode of the LIB. Carbon black Timcal Super (C45) (particle size: 20 nm, 45 $\text{m}^2 \text{g}^{-1}$), carbon nanofibers (CNF), ($D \times L$ 100nm \times 20-200 μm , 24 $\text{m}^2 \text{g}^{-1}$) and paraffinic oil were all purchased from Sigma-Aldrich, USA.

2.2. Filaments formulation

The PP powder was mixed thoroughly with the desired amount of LFP, C45, CNF and paraffinic oil in a mortar. An extruder Filabot Original supplied by Filabot Triex LLC, USA was subsequently fed with the afore-mentioned pre-mixed powder in order to obtain a standard 1.75 mm diameter 3D-printing filament. The extruder temperature was set at the relatively high temperature of 250 $^\circ\text{C}$, thereby obtaining a satisfactory extrusion rate. The filament released from the extruder nozzle was subsequently rolled around a spool by using a Filabot spooler (Filabot Triex LLC, USA). The extruder was purged thoroughly with pure PP before extrusion of each sample. Electrode filaments were kept in appropriate storage conditions under low temperature and in confined environment with low humidity.

2.3. Thermoplastic ME printing

Electrodes 3D models were designed using Autodesk Fusion 360 software after which they were divided into two-dimensional, 0.1 mm thick slices using PrusaSlicer software. 11 mm diameter positive electrode discs (200 μm and 1mm thick) and specimens ISO527-2 were printed by using a Prusa MK3 3D-printer (Prusa Research, Czech Republic) to perform further galvanostatic, electrochemical impedance spectroscopy (EIS) and mechanical tests. Nozzle standard input and output diameters of respectively 1.75 mm and 0.4 mm were used. The highest resolution in the Z direction is 0.20 mm for the first layer and 0.05mm for the following. The nozzle temperature was set at 250 $^\circ\text{C}$ and the Fan settings was set to 100%. Bed temperature was set to 100 $^\circ\text{C}$ in order to enhance the adherence of the first printed layer. Prior to printing of each sample, the nozzle was cleaned thoroughly by printing a 2 cm^3 purge cube with the corresponding filament.

2.4. Polymer PBF printing

The 3D models of the electrodes were designed with FreeCAD v.0.16 followed by slicing into 0.08 mm thick slices with Slic3r v. 1.2.9. Subsequently, 11 mm diameter electrodes discs (about 3 mm thick) and specimens ISO527-2 were printed with a Sharebot SnowWhite PBF 3D printer. The printing parameters were the following for all produced PBF objects: laser power 100 % (of maximum of 14 W), laser scan rate 25 000 (1000 mm s^{-1}), powder temperature 122 $^\circ\text{C}$, powder layer 0.25 mm, wait time 600 s, wait layer 12 s, warming layers 20, layer thickness 0.08 mm. Powder temperature was kept constant through the printing processes. These low energy-demanding parameters were chosen to produce 3D-printed electrodes with relatively significant porosity. The printed objects were carefully cleaned of all non-sintered powder using pressurized air before proceeding with subsequent experiments.

2.5. Electron Microscopy

The general homogeneity and the inner material dispersion within the PP matrix of the produced electrodes was examined by employing a FEI Quanta200F (Thermo Fisher Scientific, USA) scanning electron microscope (SEM) in high vacuum mode. The secondary and backscattered images were recorded with a 5kV acceleration voltage. Transmission electron microscopy (TEM) images and Selected Area Electron diffraction (SAED) patterns were achieved with a FEI Tecnai F20 ST electron microscope operating at 200 kV. Beforehand, printed samples were cut and inserted in a capsule in which an LR white resin (Sigma-Aldrich) was added drop by drop. The resulting capsules were then placed in an oven at 70°C during 24h. A microtome (RMC Products, Boeckeler) was then used to cut the capsules in thin slices (sections) of material of 100 nm at a cutting speed of 21.5 mm sec⁻¹. Slices were finally deposited onto a holey carbon copper grid.

2.6. Mechanical characterization

Printed specimen samples in compliance with the ISO 527-2 standard were used for tensile mechanical testing on a MTS Criterion Model 43 tensile machine set with a 1 KN load cell. Tests were controlled by displacement with a speed of 2 mm min⁻¹. Five samples of each composition were tested and the average values are reported.

2.7. Electrical conductivity characterization

EIS tests were performed using a MTZ-35 frequency response analyzer and an intermediate temperature system (ITS) supplied by BioLogic, France. It is worth noting that the exact same procedure than the one reported in our anterior work was respected [7]. Inductive phenomenon from the cables were compensated by performing calibration of the empty ITS with the same cables. ME and PBF printed electrodes discs were subsequently introduced into a controlled environment sample holder to perform AC impedance measurement under air at temperatures varying from 20 °C to 60 °C (upon heating in steps of 5 °C). An excitation voltage of 0.01 V, a frequency range of 5000 Hz to 1 Hz (20 points per decade and 10 measurements per point) and a soak time of 15 minutes were applied here. Electronic conductivities and activation energy were deduced from the Nyquist and Phase-Bode plots of the complex impedance. Conductivities were calculated from the Equation 1:

$$\sigma = \frac{1}{R} \times \frac{d}{A} \quad (1)$$

where d is the pellet thickness, A is the pellet surface area, and R is the respective resistances determined from the Nyquist and Bode plots.

2.9. Electrochemical characterization

Inside an argon filled glovebox (H₂O < 0.1 ppm, O₂ < 0.1 ppm), Swagelok-type cells were assembled. Metallic lithium was used as counter/reference electrode for half-cells while samples as working electrode. The fiber glass separator was provided by Whatman, GE Healthcare, USA. 150 µL of 1M LiPF₆ in ethylene carbonate and diethyl carbonate (EC:DEC 1:1 weight ratio) was used as electrolyte and supplied by Merck KGaA, Germany. Cells were galvanostatically charged (delithiation) and discharged (lithiation) at different current densities calculated per gram of active material, between 3.8 and 2.6 V (vs Li/Li⁺) by means of a BCS-805 (BioLogic, France). Electrochemical tests were performed at 20°C.

3. Results and discussions

3.1. Printing of positive electrodes of the same composition via PBF and ME

The preliminary stage of this study was dedicated to the preparation of positive electrodes of the same composition through PBF and ME. From classical and widely commercially employed battery materials, positive electrode samples containing 26wt% LFP as active material, 4wt% carbon black (C45) as conductive additives and 70wt% PP as polymer matrix were prepared via PBF and ME. This particular composition was chosen as it corresponds to the highest loading of charges (active material + conductive additives) allowed by the PBF technique considering the

aforementioned low energy printing parameters. In this case, the loading of charges was maximized in order to enhance the electrochemical performances while still maintaining suitable mechanical properties for further handling and characterization. Experiencing a larger amount of charges was found to immediately result in major mechanical strength and printability issues using the predetermined printing parameters. The highest loading for ME is driven by the rheology of the filled polymer, the strength and the softness of the filament while the required mechanical strength allowing the handling of the final part is the main constraint limiting the loading for PBF technique. The desired amount of each material was weighed and pre-mixed in a mortar in order to guarantee precise mixing. The resulting homogeneous powder mixture was directly inserted to feed the PBF bed during printing. While applying the defined settings, only thick electrode (3mm) discs were possible to achieve with mechanically durable electrodes.

For the alternative AM process of ME, a composite thermoplastic filament was prepared to feed the printer. Hence, the afore-mentioned pre-mixed homogeneous powder was inserted into an extruder and a first PP/LFP/C45 filament was obtained. Due to the poor diameter consistency, the latter was pelletized and extruded again, resulting in a second filament with a much more reliable diameter (1.75 mm) as confirmed through SEM before printing. Via ME printing, obtained electrodes were about 170 μm thick due to the first layer resolution limitation. Finally, it is important to mention that warping tends to occur while printing PP filaments. The material shrinkage, while 3D printing, causes the corners of the print to lift and detach from the build plate. To reduce this unfavorable effect with the PP/LFP/C45 composite, a heated bed set at 100°C and covered with adhesive tape was employed.

3.2. Characterization of electrodes of same composition obtained via PBF and ME

3.2.1. Electrical conductivity characterization

For samples obtained from both PBF and ME with the same targeted composition (26wt% LFP, 4wt% C45 and 70wt% PP), the influence of the AM process on the electrode conductivity was investigated by EIS. The corresponding impedance spectra were recorded from 20 °C to 60 °C. Nyquist and Bode plots portray typical behavior of an electronic conductor. Indeed, only Z' real part is depicted on the Nyquist plot whereas $|Z|$ magnitude is constant for all frequencies. For both tested samples, the electrical conductivity is increasing with temperature as exhibited in Figure 2, and the homogeneous activation energy values equal to 0.101 eV (PBF) and 0.099 eV (ME) were calculated. From the results obtained, it can be clearly observed that depending on the printing technique, the electrodes depict very distinctive electrical performances. Here, electrode discs obtained by means of PBF, display electronic conductivity values about 30 times higher than the electrodes printed via ME, on the whole recorded temperature range. Indeed, respectively at 20°C and 60°C, the PBF sample reveals a conductivity of 2.12×10^{-4} and $3.39 \times 10^{-4} \text{ S.cm}^{-1}$ while the ME sample exhibits a much lower conductivity equals to 7.16×10^{-6} and $1.12 \times 10^{-5} \text{ S.cm}^{-1}$. Due to the LFP and PP insulating behavior in addition to the relatively low quantity of conductive additives, these values still remain relatively low in comparison with our previous study involving a much higher loading of carbon black (up to 9 wt.% of the total composite) dispersed in a LFP/PLA positive electrode and exhibiting electronic conductivity up to 0.16 S.cm^{-1} at 20°C [8]. The incorporation of carbon additives such as C45 is crucial to confer suitable electronical conductivity.

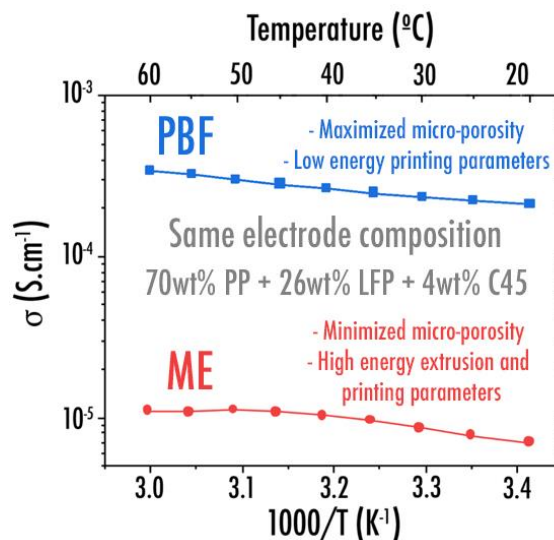


Figure 2. Arrhenius plots of the electronic conductivity for electrode of the same composition (70wt%PP + 26wt%LFP + 4wt%C45) printed via PBF and ME respectively.

3.2.2. Electron microscopy

The conductivity difference observed between both processes can be easily explained with the images revealed by SEM and TEM depicting two completely different microstructures (Figure 3). The PBF sample is composed of spherical PP polymer particles (70 μm) that were incompletely fused together on the surface during the sintering process (Figure 3a). This was possible by fine-tuning the printing parameters in a low energy configuration. During the printing procedure, an important porosity with voids is created and a three-dimensional polymer network is clearly noticeable. Charges including the active material (LFP) and conductive additives particles (C45) are deposited on the surface of the aforementioned PP spheres. Charges do not appear to be totally encapsulated within the PP matrix but are tightly attached to the incompletely melted surface. Thus, a percolating network composed of the C45 is created along all the microstructure and led to the higher electronic conductivity values depicted via EIS. While this hypothesis cannot be confirmed via SEM as carbon black particles (20 nm) are not observable with this technique, it was confirmed by performing a TEM experiment as depicted in Figure 3b. Indeed, C45 spherical particles (Figure 4a) appear to be well dispersed between the various LFP particles. The latter are clearly identified due to their bigger size (1 μm) and crystalline olivine structure allowing the observation of the atomic arrangement (Figure 4b).

On the other hand, as expected, the ME sample microstructure does not show any apparent micro-porosity (Figure 3c). This can be explained by the relatively high extrusion and printing operating temperature (250 $^{\circ}\text{C}$). Backscattered image (Figure 3c) confirms that LFP particles are evenly distributed in the polymer matrix. Nonetheless, it is important to emphasize that an important amount of these particles seems to be isolated within the polymer matrix. These active material particles being intimately related to the final electrochemical performance represents an important challenge. Indeed, isolated active material particles within the polymer matrix will act as electrochemically dead-material within the final electrode. Likewise, by performing TEM experiments (Figure 3d), it can be seen that the carbon black particles are also secluded within the PP matrix. Hence, it has obviously a detrimental effect on the percolating network and leads to the very low electronic conductivity observed previously by EIS.

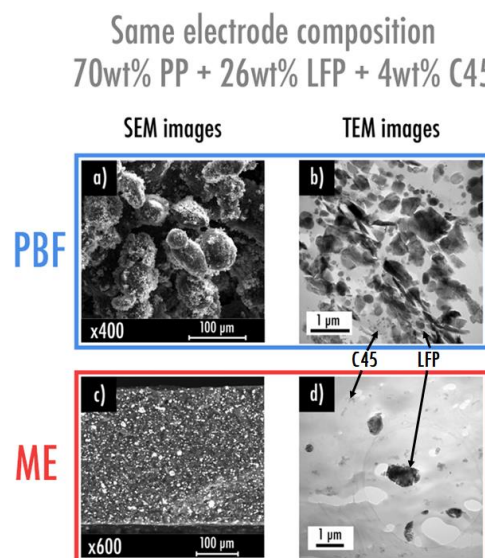


Figure 3. Cross-sectional images of the electrodes with the same composition (70wt%PP + 26wt%LFP + 4wt%C45) obtained via PBF or ME: (a) Secondary electron SEM image of the PBF electrode in which spherical PP particles surfaces are covered with smaller charges particles consisting of LFP and C45; (b) TEM image of the PBF electrode where carbon black C45 (smaller grey particles) is homogeneously distributed between the LFP particles (bigger black particles) thus creating an efficient percolating network; (c) Backscattered SEM image of the ME electrode in which LFP particles (white color) are isolated within the polymer matrix; (d) TEM image of the ME electrode where carbon black C45 (smaller grey particles) and LFP (bigger black particles) are completely isolated within the nano-porous polymer matrix.

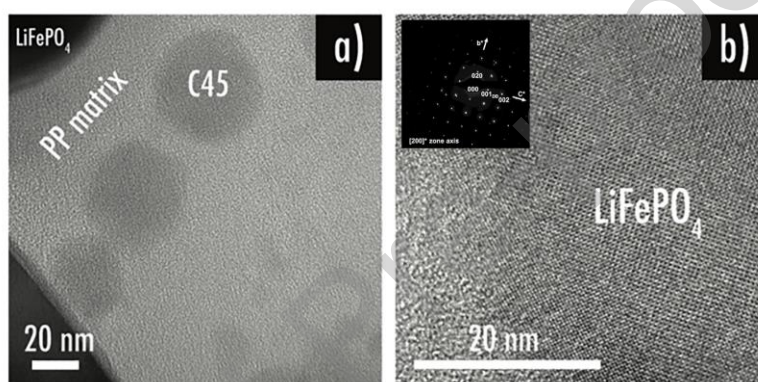


Figure 4. Cross-sectional TEM images of the PBF electrode: (a) carbon black C45 spherical particles are well dispersed between the LFP particles; (b) olivine LFP atomic arrangement. a* zone axis SAED pattern is displayed in inset (LFP: Pnmb space group; $a=6.018\text{\AA}$, $b=10.34\text{\AA}$, $c=4.703\text{\AA}$).

3.2.3. Electrochemical characterization

The electrochemical performances of the electrodes obtained by PBF and ME were investigated. The potential profiles versus the specific capacity based on the active material, and specific capacity versus cycle number were studied thoroughly at various current densities (2.1, 4.2, 8.5, and 17 mA g⁻¹ of active material corresponding respectively to C/80, C/40, C/20 and C/10) as displayed in Figure 5. Due to the important micro-porosity and higher electronic conductivity, the PBF sample exhibits, logically, higher electrochemical performances. The latter depicts an important irreversible capacity during the first cycle of 74 mAh g⁻¹ of LFP corresponding to a percentage loss of 65% at current density of 2.1 mA g⁻¹ and reversible capacity values of 35, 30, 20 and 2 mAh g⁻¹ of LFP during five cycles at current density of 2.1, 4.2, 8.5, and 17 mA g⁻¹ respectively. When finally coming back at a lower current density of 8.5 mA g⁻¹, a good capacity retention was preserved. While the electrode depicts a promising and undeniable electrochemical response, it is important to note that values are still far from the theoretical specific capacity of LFP (170 mAh g⁻¹). Moreover, considering that the total printed composite electrode is composed of only 26wt.% of active material (LFP), it means that the electrochemical performances reported per gram of total composite are much lower (reversible capacity of 9.1, 7.8, 5.2 and 0.5 mAh g⁻¹ of total composite at current density of 2.1, 4.2, 8.5, and 17 mA g⁻¹ respectively). On the other hand, the ME sample, due to the lack of micro-porosity and aforementioned isolated charges within the polymer matrix, depicts insignificant specific capacity values. The nano-porosity that was observed through TEM does not seem accessible to the lithium ions.

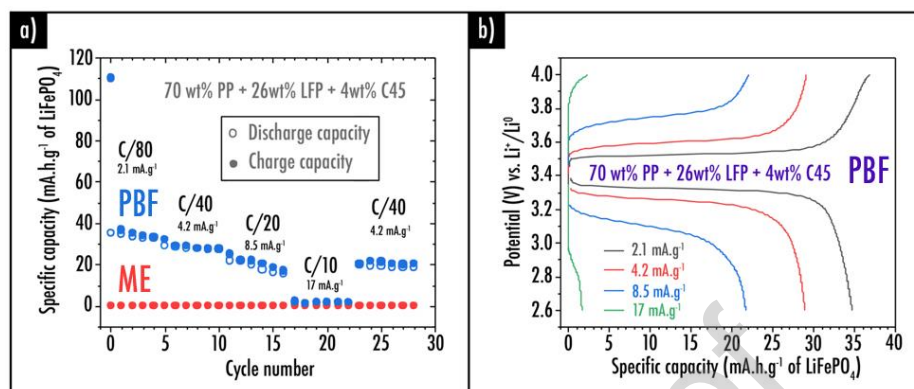


Figure 5. (a) Capacity retention plots at various current density for printed electrodes via PBF and ME for composition containing 70wt%PP + 26wt%LFP + 4wt%C45; (b) Charge/discharge capacity profiles for the electrode printed via PBF (70wt%PP + 26wt%LFP + 4wt%C45).

3.2.4. Mechanical characterization

Tensile strength experiments were performed on both the ME and PBF printed specimens based on composition (70%PP + 26%LFP + 4%C45). As depicted in Table 1, classical mechanical properties such as the Young's modulus, tensile strength and elongation at break were calculated from the stress-strain curves (Figure 6a). Obtained values logically corroborate the previous observations completed by microscopy. Samples printed with both AM technologies exhibited brittle behavior. Compared with pure PP, a drastic decrease of the elongation at break is observed of respectively 97% for the PBF sample and 94% for ME. This phenomenon can be explained by the addition of charges, known to decrease the elongation at break of a reinforced polymer. Regarding the Young's modulus and the tensile strength, it appears that both parameters corresponding to the PBF sample are lower than the ones obtained with ME for the same composition. While the tendency observed for the ME sample is classical (increase of the Young's modulus and decrease of the tensile strength in comparison with pure PP reference), the PBF sample with the exact same composition shows degraded properties due to the significant micro-porosity.

Table 1. Mechanical properties for printed electrodes of different composition.

Sample name (composition in wt%)	Young's modulus (MPa)	Tensile strength (MPa)	Elongation at break (%)
Pure PP	1400 ± 100	25 ± 1	50 ± 10
PBF – 70%PP + 26%LFP + 4%C45	284 ± 38	2.55 ± 0.41	1.39 ± 0.13
ME – 70%PP + 26%LFP + 4%C45	1468 ± 124	20.78 ± 1.28	2.87 ± 0.07
ME – 45%PP + 45%LFP + 10%C45	1435 ± 113	17.55 ± 2.50	2.88 ± 0.63
* ME – 33%PP + 49%LFP + 13%Paraffinic oil + 5%C45	485 ± 48	8.17 ± 0.55	4.73 ± 0.66

* During the extrusion and printing processes, paraffinic oil acting here as a plasticizer is partially evaporated leading to an even higher percentage of charges considering the total composite electrode.

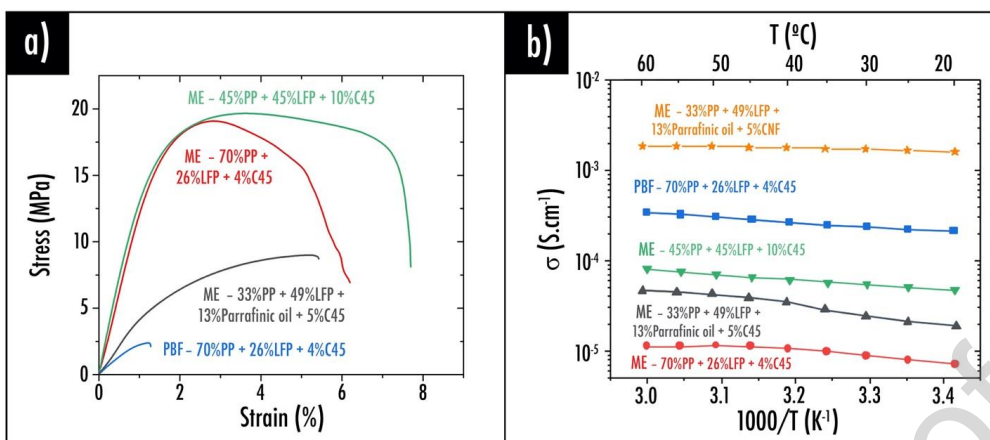


Figure 6. (a) Strain-stress curves and (b) Arrhenius plots of the different composition electrodes printed by PBF and ME.

3.3. Towards higher charge loading via ME

3.2.5. Formulation

The summary of the electrode compositions produced via ME and PBF are reported in Table 2. Distinct from what was observed previously using the PBF process (maximum of 15 vol.% of charges allowed among the total composite with the aforementioned low energy printing parameters), it was possible via ME (extrusion and printing parameters unchanged) to increase further the amount of charges without affecting the filament printability. Indeed, from our past experiences with ME [7, 8], in order to obtain sufficient mechanical performances to be printed, the total amount of charges (sum of active material and conductive additives) within the filament can reach up to 30 vol.%. This percentage can be further increased due to the introduction of an appropriate plasticizer, thus resulting in a final total amount of charges increasing to 50 vol.% [7]. Paraffinic oil, being traditionally used as plasticizer for PP [41], was employed in order to enhance the charge loading within the total composite electrode filament and facilitate printability. During both extrusion and printing processes, paraffinic oil is partially evaporated. Hence, this phenomenon leads to a higher percentage of charges when the final printed electrode composition is considered.

Table 2. Summary of the printed electrodes composition.

Printed via PBF and/or ME	Wt.% total composite PP/LFP/Plasticizer/Conductive additive	Vol.% total composite PP/LFP/Plasticizer/Conductive additive	Volumetric mass loading (mg of active material per cm ³ of the total composite)
PBF and ME	70/26/0/4	85/13/0/2	PBF: 151 mg/cm ³ ME: 202 mg/cm ³
ME	45/45/0/10	66/27/0/7	343 mg/cm ³
ME	*33/49/13/5	*48/29/13/3	*668 mg/cm ³

* During the extrusion and printing processes, paraffinic oil acting here as a plasticizer is partially evaporated leading to an even higher percentage of charges considering the total composite electrode. For weight-volume conversion, materials densities were acquired by helium pycnometer.

3.2.6. Mechanical characterization

From the mechanical perspective, as expected, the addition of charges has an unfavorable outcome on the resulting mechanical strength of the printed electrodes (Table 1). An increase of the LFP weight content from 26% to 45% leads to a small evolution of the mechanical properties. In addition, a low decrease of the Young's modulus is observed while an increase should be obtained. All these observations (mechanical properties and SEM analysis) draw the same conclusions that the mechanical behavior is driven by the properties of the interface between the charges and the matrix. With the introduction of paraffin oil as plasticizer, Young's modulus and tensile strength tend to decrease while elongation at break increases in good agreement with literature [41]. Although the resulting Young's modulus is relatively small, the subsequent filament is stiff enough to be printed. The minimum Young modulus of the filament leading to the buckling can be evaluated from the Euler's formula [28]:

$$E > \frac{64 \cdot F \cdot L^2}{\pi^3 d^4}$$

Where F is the force applied to the filament (50 N), d the diameter of the filament (1.75 mm) and L the distance between the driven gears and the top of the print head (3 mm). From these characteristics, the Young modulus to avoid buckling here must be higher than 100 MPa.

3.2.7. Electrical conductivity characterization

As revealed in Figure 6b depicting the Arrhenius plots of the electrical conductivity for each sample, C45 particles tend to be less isolated within the polymer matrix for ME specimens containing a higher amount of charges, thus resulting in a more efficient percolating network conferring higher electronic conductivity values ($4.73 \times 10^{-5} \text{ S cm}^{-1}$ at 20°C for sample “ME – 45%PP + 45%LFP + 10%C45” in comparison with $7.16 \times 10^{-6} \text{ S cm}^{-1}$ for the sample “ME – 70%PP + 26%LFP + 4%C45” at the same temperature). Nonetheless, the addition of paraffinic oil, expected to create a micro-porosity through its evaporation during printing, does not seem to have an important and effective impact on the final electronic conductivity ($1.88 \times 10^{-5} \text{ S cm}^{-1}$ at 20°C for sample “33%PP + 49%LFP + 13%Parrafinic oil + 5%C45”). Values obtained are still much lower than depicted for the “PBF – 70%PP + 26%LFP + 4%C45” sample ($2.12 \times 10^{-4} \text{ S cm}^{-1}$ at 20°C). Consequently, while C45 additives are effectively used to improve the electronic conductivity, their final contribution within the ME electrodes is not optimal. This difficulty in obtaining an efficient percolating network within the ME sample can be explained by the size of the C45 particles which is only about 20 nm as measured in the TEM images (Figure 4a). These particles are not all connected between each other, thus resulting in still relatively low conductivity. On the contrary, the introduction of bigger conductive particles would increase the probability to achieve an efficient percolating network. Hence, C45 additive is apparently not appropriate for the non-porous ME samples and a decision was made to incorporate larger CNF (about 20-200 μm long with a diameter of 100 nm). The exact same compositions were thus tested via ME using CNF instead of C45. As expected, the introduction of CNF enhances the electronic conductivity values considerably, up to $1.60 \times 10^{-3} \text{ S cm}^{-1}$ at 20°C for sample “33%PP + 49%LFP + 13%Parrafinic oil + 5%CNF”. In addition to the enhanced percolating network, the use of CNF was usually reported to decrease the viscosity of the filled polymers thus facilitating the printing by ME [42]. Besides, the incorporation of a small fraction of CNF within a polymer matrix is generally expected to enhance the mechanical performances [43]. Nonetheless, here, mechanical performances are strongly driven by the high loading of charges (up to 49%wt of LFP). Introduction of a such a small fraction of CNF, is thus not expected to improve considerably the mechanical strength. In a future work, investigations must be performed to determine if the introduction of CNF enhances the adhesion between printed layer.

3.2.8. Electrochemical characterization

Finally, investigations were focused on galvanostatic cycling to improve the understanding of the charge loading on the electrochemical performance. While samples comprising of a higher loading of active material and conductive additives (“ME – 45%PP + 45%LFP + 10%C45” and “ME – 33%PP + 49%LFP + 13%Parrafinic oil + 5%CNF”) were expected to display highly increased performance, instead, insignificantly higher specific capacity values were barely attained in comparison with what was observed beforehand (Figure 5) for reference sample “ME – 70%PP +

26%LFP + 4%C45". These poor performances can be justified by the lack of micro-porosity, caused in part by non-adequate printing parameters and minimal plasticizer evaporation, but also due to the chemical aversion of the liquid electrolyte with the PP polymer matrix. Indeed, it is well-known that within the electrolyte, Li^+ are solvated by around 4 EC molecules to form complexes [44]. Upon cycling, under the applied electric field, these latter are driven through the liquid electrolyte from an electrode to the other. Li^+ desolvation process is thus required to allow these ions to enter correctly the active material. In our previous studies [7, 8], a polar polymer matrix (PLA) was employed, containing an electron withdrawing group $\text{C}=\text{O}$ enabling to solvate Li^+ and having an affinity with the polarized molecules of EC. Hence, PLA was prone to absorb the liquid electrolyte, thus promoting samples ionic conductivity and electrochemical performances under cycling. However, here, the employed PP polymer matrix does not contain any polar groups thus conferring poor affinity with the polar molecules contained in the liquid electrolyte. The 3D-printed PP-based electrodes do not swell when soaked in the liquid electrolyte, resulting in poor ionic conductivity and specific capacity upon cycling.

3.3. Towards the future PBF and ME independent electrode optimization

3.3.1. PBF electrodes

In this work, the preparation of the PP-based positive electrodes through PBF was performed while setting printing parameters in a "low energy configuration" in order to maximize the micro-porosity and favor the electrochemical performance (Figure 7). So far, due to the laser power which was kept relatively low, the PP particles were sintered in such a way that only their surfaces were partially melted. Charges being evenly distributed on the PP particles surface, active material particles (LFP) were easily accessible by the liquid electrolyte favoring electrochemical performances under cycling while C45 created an efficient percolating network leading to good electronic conductivity of the electrode. Hence, as highlighted in the previous experiments, PBF seems to be a promising technique to print highly micro-porous electrodes. Higher charge loadings and lower electrode thickness would require selecting appropriate printing parameters such as a higher laser power, longer exposition time and higher local temperature to reach the best compromise between electrochemical and mechanical properties. In a future study, the impact of these parameters on the resulting electrode performances could be investigated.

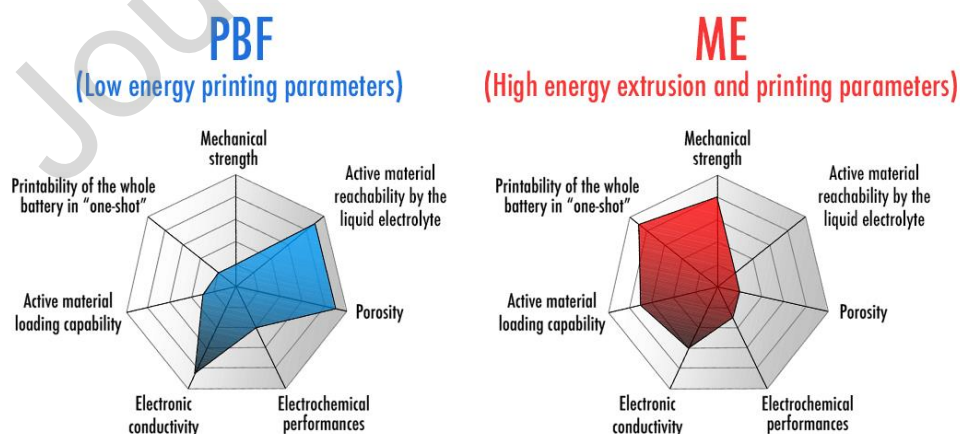


Figure 7. Summary of the advantages/drawbacks of PBF (in a low energy printing parameters configuration) and ME (in a high energy extrusion and printing parameters configuration) for the LIB printability.

3.3.2. ME electrodes

The preparation of the positive electrodes through ME was completed while setting parameters in a “high energy configuration” in order to ease the extrusion and printing processes and favor the mechanical properties (Figure 7). Unfortunately, even if the introduction of a high number of charges were possible via ME, the electronic conductivity and electrochemical performances under cycling would be drastically limited due to the LFP and conductive particles isolation within the PP polymer matrix. While we demonstrated in our previous studies [7, 8] that a micro-porosity could be created by introducing a plasticizer, paraffinic oil which was utilized here to plasticize PP does not appear to be sufficiently effective. This behavior is different than what was observed in our previous works [7, 8], in which the addition of poly(ethylene glycol) dimethyl ether average Mn~500 (PEGDME500) to plasticize PLA tends to create an important micro-porosity after extrusion and printing steps. Indeed, it was demonstrated that PEGDME500 partially evaporates during both steps but continues over time, thus creating a micro-porosity leading to an enhanced ionic conductivity and better electrochemical performance under galvanostatic cycling. Hence, future research will be dedicated to identifying the appropriate plasticizer for PP to create a significant micro-porosity capable to be filled with electrolyte or to find a plasticizer capable of absorbing electrolyte. The introduction of a polar matrix coupled with the addition of ceramic nanoparticles such as SiO₂ or Al₂O₃ within the electrodes could also enhance the electrolyte impregnation. In parallel, an in-depth optimization of the extrusion and printing temperatures must be achieved in a future work in order to achieve the best compromise between mechanical and electrochemical performances. Finally, while ME is currently widely used in many fields, various technical issues such as the thermoplastic filament-shape requirement and low resolution (200 μm for the first layer) remain challenges to overcome in order to facilitate its use in the battery manufacturing. The in-plane resolution is mainly controlled by the diameter of the nozzle while the out-of-plane resolution (according to z symbol for the thickness of the layers) is conditioned by the resolution of the printer and the viscosity of the fused material. In our previous articles [7, 8], it has indeed been demonstrated that with the exception of the first layer, the above layers can be printed with a thickness down to 50 μm. In contrast, in the plane, a nozzle with a diameter of 0.4 mm was used, allowing improved resolution. In practice, it can be envisaged to use nozzles with smaller diameters (down to 0.1 mm). However, the high viscosity of the filled polymers but also a large diameter of the fillers (greater than 0.1 times the diameter of the nozzle) can lead to clogging of the nozzle [45]. With the objective of improving the overall system, next step would be to use the future optimized current collector filament in order to print the first layer subjected to the 200 μm thickness limitation [27]. Hence, it would be possible to print thinner (down to 50 μm) and balanced electrodes on top of it and thus further improve the electrochemical performances.

3.4. Considering the future printability of the complete LIB

3.4.1. Electrochemical simulation of LIB electrodes architectures

Battery performances can be evaluated based on different characteristics such as the capacity Q (Ah), the energy W (Wh) and the power P (W). These values can be scaled as volumetric, areal, or gravimetric densities. To improve the performances of a battery for a given composition of the electrodes (amount of the active particles, porosity) and to find a tradeoff between power and energy, it is necessary to propose new designs that varying the shapes and the sizes of the electrodes and the volume fraction between the electrodes and electrolyte. Long et al. [20] have given a classification of the different potential designs based on the diffusion path (1D, 2D and 3D). To show the advantages of a 3D architectures, several Periodic Unit Cells (PUC) are studied (Figure 8). Four types of PUC are considered:

- a) *Planar*: Interdigitated plate array of cathode and anode. Although this architecture is 3D, it will be classified as 1D because Li⁺ ion diffusion occurs only in one direction perpendicular to the surfaces of the electrodes.
- b) *Interdigitated*: Arrays of alternating cylindrical cathodes and anodes are classified as 2D diffusion.
- c) *Cube*: Two interlaced arrays of electrodes [23]. In this case, ion diffusion is homogeneous and occurs in the three directions.
- d) *Gyroid*: A double-gyroid cubic unit cell which is triply periodic [46]. The interfaces are defined by the following double surface:

$$\sin\left(\frac{2\pi}{L_C}x\right)\cos\left(\frac{2\pi}{L_C}y\right) + \sin\left(\frac{2\pi}{L_C}y\right)\cos\left(\frac{2\pi}{L_C}z\right) + \sin\left(\frac{2\pi}{L_C}z\right)\cos\left(\frac{2\pi}{L_C}x\right) = \pm t$$

With L_C the cubic unit cell length and $0 < t \leq 1.413$

For each considered PUC, the type of diffusion path, the surface area (S_a), the volume (V_a) and the volume fraction (V_f) of the electrode but also the S_a/V_a are given (Table 3).

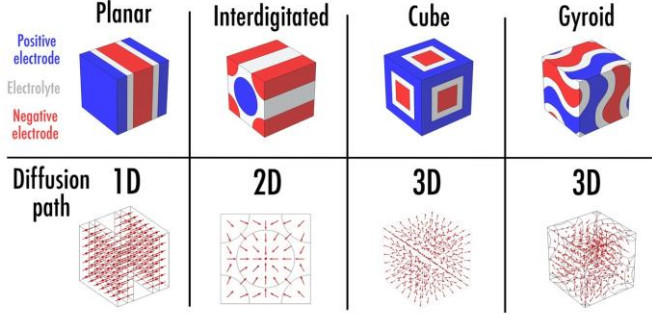


Figure 8. Summary of the investigated periodic unit cells and their respective Li^+ diffusion path. While commercial LIB consist in parallel plates (planar design), complex LIB architectures (interdigitated, cube, gyroid) could be obtained through AM processes.

Table 3. Characteristics of the unit cells.

Type	Planar	Interdigitated	Cube	Gyroid
Surface Area S_a	$S_a = 2L_C^2$	$S_a = 2\pi aL_C$	$S_a = 12a(L_C - a)$	Depends on t
Electrode Volume V_a	$V_a = aL_C^2$	$V_a = \pi a^2L_C$	$V_a = 3a^2L_C - 2a^3$	Depends on t
S_a/V_a ratio	$S_a/V_a = \frac{2}{a}$	$S_a/V_a = \frac{2}{a}$	$S_a/V_a = \frac{12(L_C - a)}{3aL_C - 2a^2}$	Depends on t
Electrode Volume fraction V_f	$V_f = a/L_C$	$V_f = \pi a^2/L_C^2$	$V_f = \frac{3a^2L_C - 2a^3}{L_C^3}$	Depends on t ($t=0.64$ for $V_f=0.325$)

To respect balancing between the anode and cathode, the volume of the electrodes is assumed to be equal leading to the following cubic unit cell length L_C defined as $L_C = 2a + 2e$ where a and e are respectively the thickness of an electrode and the electrolyte (in the case of interdigitated cylindrical electrodes a is the radius of the electrode and $2e$ the smallest distance between two adjacent anodes or cathodes). As the performance of a battery depends on different parameters, several can be fixed by considering the same materials volume fractions across the unit cell (cathode/anode/electrolyte volume fractions equal to 0.325/0.325/0.35) and the same size of the unit cell ($L_C=300 \mu\text{m}$).

To evaluate the electrochemical performances (capacity, energy and power) of the different configurations, the governing equations defined in Table 4 must be solved. In this article, a homogenized approach is used for

describing porous electrodes [47], which solves simultaneously for the electrode phase and electrolyte phase potentials in the same domain, defining the electrode reactions by the use of source terms. The lithium diffusion into the solid electrode particles is modeled by the use of an extra dimension, representing an average particle for a certain position in the electrode [48]. Other models consider electrodes as non-porous and Li^+ insertion is described by the boundary conditions, not as source term, resulting in a slightly modified mathematical description [24, 49]. In this paper, Comsol Multiphysics 5.5 finite element software was used to solve the equations. To study the unit cell discharge behavior, a generalized α -integrator in conjunction with PARDISO solver was used to solve time dependent matrix equation. The relative and absolute tolerances were equal to 0.001. Following the applied C-rate, a different maximum time step was applied (automatic one for C-rates less than 1 and 1s for C-rates higher than 1). The geometries were discretized automatically using a physics-controlled mesh with normal size leading to approximately 80,000 quadratic second order tetrahedral elements and 10,500 triangular elements for the interfaces. Calculations were performed on a Dell Workstation equipped with 32 cores on Intel Xeon 5680 processors and a memory of 64 Gb.

Journal Pre-proof

Table 4. Electrochemical model Equations.

Governing Equations	Hypotheses
<p>Conservation of Li⁺ species for a binary salt concentrated electrolyte</p> $\varepsilon_m \frac{\partial c_l}{\partial t} = D_{eff,m} \nabla^2 c_l + (1 - t_+) j_m$ <p>$m = p \text{ or } n \text{ or } s$ (p=positive, n=negative, s=separator)</p>	<ul style="list-style-type: none"> • Solvent velocity equals to zero • Constant transport properties • Constant porosity • Structural properties-porosity integrated in $D_{eff,m} = D_e \varepsilon_m^{1.5}$
<p>Charge conservation in solution (electrolyte phase)</p> $\nabla \cdot (-\kappa_{eff,m} \nabla \Phi_l + \kappa_{D,m} \nabla \ln c_l) = F j_m$ <p>With $\kappa_{D,m}$ diffusional conductivity $\kappa_{D,m} = \frac{2\kappa_{eff} RT}{F} (1 - t_+)$</p>	<ul style="list-style-type: none"> • Structural properties-porosity integrated in $\kappa_{eff,m} = \kappa \varepsilon_m^{1.5}$ • No reaction in the separator
<p>Potential distribution in solid phase</p> $\sigma_{eff,m} \nabla^2 \Phi_s = F j_m$	<ul style="list-style-type: none"> • Structural properties-porosity integrated in $\sigma_{eff,m} = \sigma_s \varepsilon_{am}$
<p>Conservation of Li⁺ species in solid phase</p> $\frac{\partial c_s}{\partial t} = \frac{1}{r} \frac{\partial}{\partial r} \left(D_m r \frac{\partial c_s}{\partial r} \right)$	<ul style="list-style-type: none"> • Spherical particles with a radius of 1 μm • Uniform size and distribution of particles
<p>Reaction rate at the surface of particles (Butler-Volmer equation)</p> $j_m = j_{om} \left(\exp \left(\frac{\alpha_n F}{RT} (\Phi_s - \Phi_l - U) \right) - \exp \left(\frac{\alpha_p F}{RT} (\Phi_s - \Phi_l - U) \right) \right)$	

In this paper, the LFP-graphite system is studied. Literature and adjusted data were reported in Table 5. The porosities and the active material volume fractions were collected from our research works on 3D printing of electrodes by ME [7, 8]. The initial SOCs were defined considering a charge balance between the cathode and the anode leading to a nominal capacity of 1.9 μAh .

Table 5. Design parameters (for $V_f=0.325$) and materials properties.

	Parameter	Symbol	Unit	Positive electrode	Separator	Negative electrode
Design specifications	Electrode feature	a	μm	97.5/96/114*		97.5/96/114*
	Electrolyte feature	e	μm		52.5/54/36*	
	Porosity	ε_m		0.2	0.3	0.2
	Active material volume fraction	ε_{am}		0.4		0.4

Solid and electrolyte phase Li ⁺ concentration	Maximum solid phase concentration	$c_{s,max}$	mol/m ³	22806	31450
	Initial SOC	SOC _m		0.012	0.477
	Average electrolyte concentration	c_l	mol/m ³		1000
Kinetic and transport properties	Exchange current density	j_{om}	A/m ²	$5e^{-2}$	0.5
	Charge transfer coefficient	α_m		0.5	0.5
	Li transport number	t_+			0.363
	Solid phase Li diffusion	D_s	m ² /s	$3.2e^{-13}$	$1.6e^{-14}$
	Electrolyte phase Li ⁺ diffusion	D_e	m ² /s		$5e^{-10}$
	Ionic conductivity of electrolyte	κ	S/m		1.3

* corresponds to the values for planar/interdigitated/cube geometries. The dimensions are not uniform for gyroid geometry.

To compare the performances of the different geometries, a Ragone plot, exhibiting the energy versus the power, was generated (Figure 9a). With increased energy output, less power is obtained and vice versa. Clearly, it appears that the shape of the Ragone plot is affected by the battery design. Simulations were performed at different applied discharge currents corresponding to C-rates from 0.05C to 20C. The power was evaluated from the discharge time when the cut-off voltage of 2.6 V is reached. For low C-rate current loads (< 4C), all the geometries display very similar behavior. At higher C-rates, best performances are achieved with the 3D gyroid geometry while the 1D planar provides the worst. The effect on a multiaxial diffusion path can be underlined by comparing energy density for planar and interdigitated geometries for which the electrode volume and area are equal (Table 3). It can be observed that the performances between the geometries are not proportional to the applied C-rates. Compared to planar geometry, gyroid and cube respectively exhibit significantly improved energies of +158% and +115% at a rate of 6C, and +134% and +86% at 20C (Table 6). The drop in energy for a C-rate of 6C can be explained by the shape of the discharge profiles (Figure 9b). At this particular current density, the shapes of the curves for the considered geometries are different (this is due a higher gradient of concentration for planar geometry than for the other ones) although that for a 10C C-rate, the shapes of the curves are identical. Despite better performance, gyroid geometry is more complex to print for small unit cell sizes. Interlaced cube geometry seems to be a good compromise between both electrochemical performances and printability parameters. The ultimate goal of this project being to demonstrate the printability of complete LIB architectures (Figure 8) in one single, non-assembly step, the multi-material printing abilities for both AM techniques must be examined.

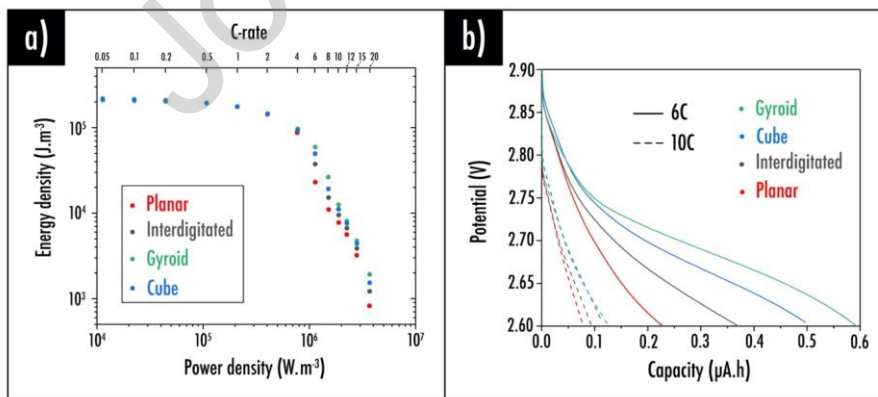


Figure 9. (a) Ragone plot for all the geometries for different C-rate; (b) Discharge profiles, potential as a function of the capacity for 6C and 10C current densities.

Table 6. Energy density improvement (%) for the different geometries compared to the planar geometry.

C-rate	Interdigitated	Cube	Gyroid
C/20	0.0%	0.0%	-4.2%
C/10	0.0%	0.0%	-3.8%
C/5	0.0%	0.1%	-3.0%
C/2	-0.1%	0.1%	-0.7%
C	-0.3%	0.2%	0.5%
2C	-0.5%	0.3%	1.4%
4C	-1.9%	4.4%	9.0%
6C	62.4%	115.1%	158.2%
8C	38.0%	73.8%	139.7%
10C	22.6%	42.7%	61.4%
12C	18.6%	35.4%	43.8%
15C	19.7%	37.3%	47.4%
20C	48.1%	86.5%	134.2%

3.4.2. Multi-material PBF

Few studies have been reported in literature on LIB PBF 3D-printing precisely as this PBF printing technique does not allow printing the full battery in one single print (“one shot”). Indeed, printability of multi-material objects via polymer, ceramic or metal PBF is not widely established currently [50]. During PBF printing, the object is completely immersed within the material powder bed, and consequently, is technically not possible for now to print an object with six different powders corresponding to each part of the battery (negative electrode, positive electrode, solid electrolyte, Cu and Al based current collectors and packaging) in one single print. One alternative for now is to print each part separately and to assemble it afterwards, or to use different manufacturing techniques for producing the parts of the LIB that are not feasible to produce via PBF (e.g. packaging). Hence, only planar or perfectly fitting printed parts can be considered. 3D complex interpenetrated architectures such as the one described in Figure 8 (interdigitated, cube or gyroid) are not achievable via PBF. Unfortunately, this kind of architecture could result in enhanced performances in terms of specific capacity and power as demonstrated in this study.

3.4.3. Multi-material ME

Relative to PBF printing, thermoplastic ME printing offers many different multi-material commercial options (Table 7) with a view to print these complete LIB complex architectures in one single step. The Canadian company Mosaic Manufacturing, founded in 2014, created Palette2S, additional box, in which up to four filaments can be combined together with a view to create a single monofilament that will be used to feed the printer (Figure 10a). While this process works well to even combine different types of materials together, such as PLA or PETG, the combination of brittle composite filaments such as the one developed to print the Li-ion battery electrodes is challenging.

Another option (Figure 10b) includes integrating several extruder-heads on the same X-axis carriage, however, nozzles are not free to move independently. The first challenge is regarding nozzle temperature control. Indeed, when considering the LIB complete printing, it is important to emphasize that printing temperature for each filament will be different and thus nozzles temperature needs to be thoroughly controlled independently. Imagining that this issue could be easily resolved by tuning the printer firmware, another issue appears: the retraction parameters. Indeed, filament residuals generally continue extruding from the nozzle when not printing. This issue is really problematic when the LIB printing is considered as it may result immediately in short-circuits if residue from the negative electrode filament are in contact with the positive electrode.

Third option involves the use of independent nozzles (Figure 10c). While dual independent extruders already exist and can be found widely in the market, the ability to have more than 2 nozzles is not widely established due to the complexity to control movement and nozzles temperature independently. Moreover, very often, this option involves independent extruders that are placed on the same X-axis thus reducing considerably the printing area. A solution would consist to have all-axis-independent extruders that could be placed in mechanically controlled arms; unfortunately, this option still remains too expensive.

Finally, the last option to print a complete LIB via ME was developed by the Czech company Prusa Research. Their option called MMU2S is based on an additional device (Figure 10d), placed on the top of the printer, that will act as filament selector. A motor operates an idler and selects which bearing will engage the drive gear to push the filament. A second motor rotates all of the drive gears. At any given time, only one motor pushes the filament farther, depending on the idler rotation. A third motor moves the selector. The latter aligns with the path of one of the five filaments so that it can be sent to the extruder. A mechanical P.I.N.D.A probe is used as a filament sensor during each filament change to detect proper filament load and unload. The filament is advanced by the Bondtech gears and reaches the nozzle. This option seems to be the most promising to entirely print the future all solid-state LIB in one single step as the main advantage is that only one nozzle is used. Moreover, unlike the others options involving many nozzles, the calibration on the Z axis is relatively uncomplicated to perform. To deal with the material transition after filament change, an almost hollow purge tower is built in a corner of the bed. This sacrificial build unfortunately leads to material waste. Finally, this option remains relatively cheap as the printer equipped with the MMU2S option costs about \$1,000 USD.

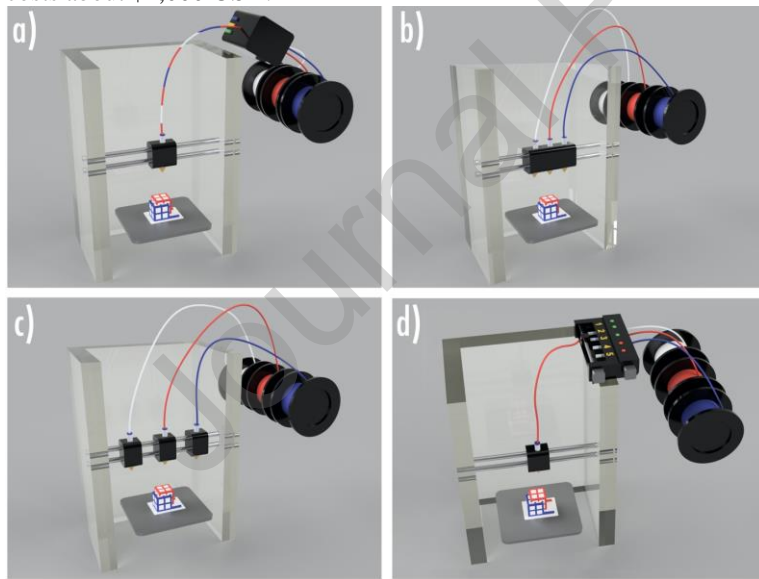


Figure 10. Summary of the ME multi-materials options available.

Table 7. Summary of the commercially available ME multi-materials options.

Technology	Product designation	Company	Price (€)
Monofilament multi-materials	Palette 2s	Mosaic Manufacturing	<1000

Multi dependent extruder-heads (at least 3 heads)	Hydra 16 A	Hyrel 3D	27 000
Multi independent extruder-heads	S 600D	Lynxter	36 000
	Multirap M500	Multec	46 000
	3Dn-Quad-Head	Nscript	280 000
Mono extruder multifilament	MMU2S	Prusa	<1000

4. Conclusion

For the first time, the ability to 3D print PP-based LIB components through two particularly different AM processes, ME and PBF, was considered. The extrusion and printing parameters were kept unchanged from the outset: high energy extrusion and printing parameters (e.g. temperature) were set for the ME technique while low energy printing parameters were fixed for PBF. Considering these settings, it was demonstrated that resulting electrical, morphological, mechanical and electrochemical performances are significantly different for a similar electrode composition, printed via PBF or ME.

A porous 3D polymer network was created with PBF, favoring the liquid electrolyte impregnation, active material particles accessibility, and thus resulting in encouraging electrochemical performances under cycling. Charges being evenly distributed on the PP particles surface, an efficient percolating network leading to promising electronic conductivity of the electrode was also observed. On the other hand, higher loading of charges was made possible with the ME process thanks to the introduction of paraffinic oil used as plasticizer for PP. Unfortunately, the electronic conductivity and electrochemical performances under cycling appear to be significantly limited due to the LFP and conductive particles isolation within the PP polymer matrix. Future research should be devoted to finding the appropriate plasticizer for PP to create a significant micro-porosity capable to be filled with electrolyte. The introduction of a polar polymer matrix coupled with the addition of ceramic nanoparticles such as SiO₂ or Al₂O₃ within the electrodes must also be investigated to improve the electrolyte impregnation. In parallel, for both AM techniques, search for suitable conductive polymer matrix as well as a major optimization of the extrusion and printing temperatures must be accomplished in a future work to reach the best compromise between mechanical and electrochemical performances. While this study was based on classical LIB materials, future studies could be extended to any materials (active material/conductive additive/thermoplastic polymer matrix).

Furthermore, through an in-depth modeling study, it was demonstrated that innovative three-dimensional LIB architectures (gyroid, cube, interdigitated), in comparison with classical two-dimensional planar design, are particularly promising from the electrochemical point of view, at high current densities (power applications). Interlaced cube geometry seems to be a good compromise between both electrochemical performances and printability parameters. The ultimate goal of such a project being to demonstrate the printability of the complete LIB in one single, non-assembly step, the multi-material printing abilities for both AM techniques were examined. From this comparative study, it is clear that neither ME nor PBF should be eliminated hastily as both techniques present advantages and drawbacks for the LIB printability. Research routes must be kept opened for now on both techniques and especially on the development of innovative multi-materials and hybrid options that will, one day, pave the way towards an efficient liquid-based but also all-solid-state LIB 3D-printing in one-single step.

Acknowledgements

This work was supported by the Fonds Européen de Développement Régional (FEDER), the Région Hauts-de-France and the Université de Picardie Jules Verne (UPJV). The authors would like to thank the UPJV microscopy platform for sharing their facilities.

Statement on Conflicts of Interest

One of the authors of this article is part of the Editorial Board of the journal. To avoid potential conflicts of interest, the responsibility for the editorial and peer-review process of this article lies with the journal's other editors. Furthermore, the authors of this article were removed from the peer review process and had no, and will not have any access to confidential information related to the editorial process of this article.

References

- [1] E. MacDonald, R. Wicker, Multiprocess 3D printing for increasing component functionality, *Science* 353(6307) (2016).
- [2] L.E. Weiss, R. Merz, F.B. Prinz, G. Neplotnik, P. Padmanabhan, L. Schultz, K. Ramaswami, Shape deposition manufacturing of heterogeneous structures, *Journal of Manufacturing Systems* 16(4) (1997) 239-248.
- [3] A. Kataria, D.W. Rosen, Building around inserts: methods for fabricating complex devices in stereolithography, *Rapid Prototyping Journal* 7(5) (2001) 253-261.
- [4] E. Malone, H. Lipson, Fab@Home: the personal desktop fabricator kit, *Rapid Prototyping Journal* 13(4) (2007) 245-255.
- [5] C. Robinson, B.E. Stucker, A.J. Lopes, R. Wicker, J.A. Palmer, Integration of direct-write and ultrasonic consolidation technologies to create advanced structures with embedded electrical circuitry, *Solid Freeform Fabrication Symposium Proceedings*, University of Texas at Austin, 2006, pp. 60-69.
- [6] M. Navarrete, A. Lopes, J. Acuna, R. Estrada, E. MacDonald, J. Palmer, R. Wicker, Integrated layered manufacturing of a novel wireless motion sensor system with GPS, *Solid Freeform Fabrication Symposium Proceedings*, University of Texas at Austin, 2007, pp. 575-585.
- [7] A. Maurel, M. Courty, B. Fleutot, H. Tortajada, K. Prashantha, M. Armand, S. Grugeon, S. Panier, L. Dupont, Highly Loaded Graphite-Polylactic Acid Composite-Based Filaments for Lithium-Ion Battery Three-Dimensional Printing, *Chemistry of Materials* 30(21) (2018) 7484-7493.
- [8] A. Maurel, S. Grugeon, B. Fleutot, M. Courty, K. Prashantha, H. Tortajada, M. Armand, S. Panier, L. Dupont, Three-Dimensional Printing of a LiFePO₄/Graphite Battery Cell via Fused Deposition Modeling, *Scientific Reports* 9(1) (2019) 18031.
- [9] A. Maurel, M. Armand, S. Grugeon, B. Fleutot, C. Davoisne, H. Tortajada, M. Courty, S. Panier, L. Dupont, Poly(Ethylene Oxide)-LiTFSI Solid Polymer Electrolyte Filaments for Fused Deposition Modeling Three-Dimensional Printing, *Journal of the Electrochemical Society* 167(7) (2020).
- [10] A. Maurel, S. Grugeon, M. Armand, B. Fleutot, M. Courty, K. Prashantha, C. Davoisne, H. Tortajada, S. Panier, L. Dupont, Overview on Lithium-Ion Battery 3D-Printing By Means of Material Extrusion, *ECS Transactions* 98(13) (2020) 3-21.
- [11] E. Macdonald, R. Salas, D. Espalin, M. Perez, E. Aguilera, D. Muse, R.B. Wicker, 3D Printing for the Rapid Prototyping of Structural Electronics, *Ieee Access* 2 (2014) 234-242.
- [12] Y. Yang, W. Yuan, X. Zhang, Y. Yuan, C. Wang, Y. Ye, Y. Huang, Z. Qiu, Y. Tang, Overview on the applications of three-dimensional printing for rechargeable lithium-ion batteries, *Applied Energy* 257 (2020) 114002.
- [13] Y. Pang, Y. Cao, Y. Chu, M. Liu, K. Snyder, D. MacKenzie, C. Cao, Additive Manufacturing of Batteries, *Advanced Functional Materials* 0(0) (2019) 1906244.
- [14] P. Chang, H. Mei, S.X. Zhou, K.G. Dassios, L.F. Cheng, 3D printed electrochemical energy storage devices, *Journal of Materials Chemistry A* 7(9) (2019) 4230-4258.
- [15] H. Bikas, P. Stavropoulos, G. Chryssolouris, Additive manufacturing methods and modelling approaches: a critical review, *International Journal of Advanced Manufacturing Technology* 83(1-4) (2016) 389-405.
- [16] L. Chen, Y. He, Y.X. Yang, S.W. Niu, H.T. Ren, The research status and development trend of additive manufacturing technology, *International Journal of Advanced Manufacturing Technology* 89(9-12) (2017) 3651-3660.
- [17] B. Berman, 3-D printing: The new industrial revolution, *Business Horizons* 55(2) (2012) 155-162.
- [18] W. Gao, Y.B. Zhang, D. Ramanujan, K. Ramani, Y. Chen, C.B. Williams, C.C.L. Wang, Y.C. Shin, S. Zhang, P.D. Zavattieri, The status, challenges, and future of additive manufacturing in engineering, *Computer-Aided Design* 69 (2015) 65-89.
- [19] T.D. Ngo, A. Kashani, G. Imbalzano, K.T.Q. Nguyen, D. Hui, Additive manufacturing (3D printing): A review of materials, methods, applications and challenges, *Composites Part B-Engineering* 143 (2018) 172-196.
- [20] J.W. Long, B. Dunn, D.R. Rolison, H.S. White, Three-dimensional battery architectures, *Chemical Reviews* 104(10) (2004) 4463-4492.
- [21] T.S. Arthur, D.J. Bates, N. Cirigliano, D.C. Johnson, P. Malati, J.M. Mosby, E. Perre, M.T. Rawls, A.L. Prieto, B. Dunn, Three-dimensional electrodes and battery architectures, *Mrs Bulletin* 36(7) (2011) 523-531.

- [22] H.T. Sun, J. Zhu, D. Baumann, L.L. Peng, Y.X. Xu, I. Shakir, Y. Huang, X.F. Duan, Hierarchical 3D electrodes for electrochemical energy storage, *Nature Reviews Materials* 4(1) (2019) 45-60.
- [23] H. Ragonés, S. Menkin, Y. Kamir, A. Gladkikh, T. Mukra, G. Kosa, D. Golodnitsky, Towards smart free form-factor 3D printable batteries, *Sustainable Energy & Fuels* 2(7) (2018) 1542-1549.
- [24] B. Trembacki, E. Duoss, G. Oxberry, M. Stadermann, J. Murthy, Mesoscale Electrochemical Performance Simulation of 3D Interpenetrating Lithium-Ion Battery Electrodes, *Journal of the Electrochemical Society* 166(6) (2019) A923-A934.
- [25] L. Taberna, S. Mitra, P. Poizot, P. Simon, J.M. Tarascon, High rate capabilities Fe₃O₄-based Cu nano-architected electrodes for lithium-ion battery applications, *Nature Materials* 5(7) (2006) 567-573.
- [26] C. Reyes, R. Somogyi, S. Niu, M.A. Cruz, F. Yang, M.J. Catenacci, C.P. Rhodes, B.J. Wiley, Three-Dimensional Printing of a Complete Lithium Ion Battery with Fused Filament Fabrication, *ACS Applied Energy Materials* 1(10) (2018) 5268-5279.
- [27] A. Maurel, PhD Thesis - Thermoplastic composite filaments formulation and 3D-printing of a lithium-ion battery via fused deposition modeling, Université de Picardie Jules Verne, Amiens, France, 2020.
- [28] B.N. Turner, R. Strong, S.A. Gold, A review of melt extrusion additive manufacturing processes: I. Process design and modeling, *Rapid Prototyping Journal* 20(3) (2014) 192-204.
- [29] J.W. Stansbury, M.J. Idacavage, 3D printing with polymers: Challenges among expanding options and opportunities, *Dental Materials* 32(1) (2016) 54-64.
- [30] C.W. Foster, M.P. Down, Y. Zhang, X.B. Ji, S.J. Rowley-Neale, G.C. Smith, P.J. Kelly, C.E. Banks, 3D Printed Graphene Based Energy Storage Devices, *Scientific Reports* 7 (2017) 11.
- [31] S.Q. Yuan, Y. Zheng, C.K. Chua, Q.Y. Yan, K. Zhou, Electrical and thermal conductivities of MWCNT/polymer composites fabricated by selective laser sintering, *Composites Part a-Applied Science and Manufacturing* 105 (2018) 203-213.
- [32] J.H. Koo, L. Pilato, G. Wissler, J. Cheng, W. Ho, K. Nguyen, S. Lao, A. Cummings, M. Ervin, Innovative selective laser sintering rapid manufacturing using nanotechnology, Paper presented at 16th Solid Freeform Fabrication Symposium, SFF 2005, Austin, TX, United States, 2005, pp. 98-108.
- [33] S.R. Athreya, K. Kalaitzidou, S. Das, Processing and characterization of a carbon black-filled electrically conductive Nylon-12 nanocomposite produced by selective laser sintering, *Materials Science and Engineering: A* 527(10) (2010) 2637-2642.
- [34] S.C. Lao, J.H. Koo, T.J. Moon, Flammability and thermal properties of polyamide 11 - alumina nanocomposites, *Proceedings Of the 2009 SFF Symposium* . 3-5 August . Austin, TX, 2009.
- [35] S.C. Lao, J.H. Koo, W. Yong, Polyamide 11-Carbon nanotubes nanocomposites: preliminary investigation, *Proceedings of the 2010 SFF Symposium* . 2-4 August . Austin, TX, 2010.
- [36] S. Gaikwad, J.S. Tate, N. Theodoropoulou, J.H. Koo, Electrical and mechanical properties of PA11 blended with nanographene platelets using industrial twin-screw extruder for selective laser sintering, *Journal of Composite Materials* 47(23) (2013) 2973-2986.
- [37] T. Koyano, A. Hosokawa, R. Igusa, T. Ueda, Electrochemical machining using porous electrodes fabricated by powder bed fusion additive manufacturing process, *Cirp Annals-Manufacturing Technology* 66(1) (2017) 213-216.
- [38] E. Lahtinen, M.M. Hanninen, K. Kinnunen, H.M. Tuononen, A. Vaisanen, K. Rissanen, M. Haukka, Porous 3D Printed Scavenger Filters for Selective Recovery of Precious Metals from Electronic Waste, *Advanced Sustainable Systems* 2(10) (2018).
- [39] E. Lahtinen, E. Kukkonen, J. Jokivartio, J. Parkkonen, J. Virkajarvi, L. Kivijarvi, M. Ahlskog, M. Haukka, Preparation of Highly Porous Carbonous Electrodes by Selective Laser Sintering, *Acs Applied Energy Materials* 2(2) (2019) 1314-1318.
- [40] J.W. Sha, Y.L. Li, R.V. Salvatierra, T. Wang, P. Dong, Y.S. Ji, S.K. Lee, C.H. Zhang, J.B. Zhang, R.H. Smith, P.M. Ajayan, J. Lou, N.Q. Zhao, J.M. Tour, Three-Dimensional Printed Graphene Foams, *Acs Nano* 11(7) (2017) 6860-6867.
- [41] G. Wypych, Effect of plasticizers on properties of plasticized materials, *Handbook of Plasticizers: Third Edition* 2017, pp. 209-219.
- [42] S.M. Lebedev, O.S. Gefle, E.T. Amitov, D.Y. Berchuk, D.V. Zhuravlev, Poly(lactic acid)-based polymer composites with high electric and thermal conductivity and their characterization, *Polymer Testing* 58 (2017) 241-248.
- [43] M.M. Hasan, Y. Zhou, S. Jeelani, Thermal and tensile properties of aligned carbon nanofiber reinforced polypropylene, *Materials Letters* 61(4) (2007) 1134-1136.

- [44] W. Cui, Y. Lansac, H. Lee, S.T. Hong, Y.H. Jang, Lithium ion solvation by ethylene carbonates in lithium-ion battery electrolytes, revisited by density functional theory with the hybrid solvation model and free energy correction in solution, *Physical Chemistry Chemical Physics* 18(34) (2016) 23607-23612.
- [45] T. Beran, T. Mulholland, F. Henning, N. Rudolph, T.A. Osswald, Nozzle clogging factors during fused filament fabrication of spherical particle filled polymers, *Additive Manufacturing* 23 (2018) 206-214.
- [46] M.R.J. Scherer, *Double-Gyroid-Structured functional materials: synthesis and applications*, Springer Science & Business Media, 2013.
- [47] J. Newman, W. Tiedemann, Porous-electrode theory with battery applications, *AIChE Journal* 21(1) (1975) 25-41.
- [48] M. Doyle, T.F. Fuller, J. Newman, Modeling of galvanostatic charge and discharge of the lithium polymer insertion cell, *Journal of the Electrochemical Society* 140(6) (1993) 1526-1533.
- [49] V. Zadin, H. Kasemagi, A. Aabloo, D. Brandell, Modelling electrode material utilization in the trench model 3D-microbattery by finite element analysis, *Journal of Power Sources* 195(18) (2010) 6218-6224.
- [50] Y. Chivel, New approach to multi-material processing in selective laser melting, *Laser Assisted Net Shape Engineering 9 International Conference on Photonic Technologies Proceedings of the Lane 2016* 83 (2016) 891-898.

CRedit authorship contribution statement

Alexis Maurel: Conceptualization, Methodology, Investigation, Writing - original draft, Writing - review & editing. **Matti Haukka:** Investigation, Writing - original draft. **Eric MacDonald:** Investigation, Writing - original draft. **Lauri Kivijärvi:** Investigation, Writing - original draft. **Elmeri Lahtinen:** Investigation, Writing - original draft. **Hyeonseok Kim:** Investigation. **Michel Armand:** Writing - review & editing. **Aurélie Cayla:** Investigation. **Arash Jamali:** Investigation. **Sylvie Grugeon:** Investigation, Supervision, Writing - original draft, Writing - review & editing. **Loic Dupont:** Project administration, Resources, Supervision, Writing - original draft, Writing - review & editing. **Stéphane Panier:** Investigation, Project administration, Resources, Supervision, Writing - original draft, Writing - review & editing.

Declaration of interests

The authors declare that they have no known competing financial interests or personal relationships that could have appeared to influence the work reported in this paper.

The authors declare the following financial interests/personal relationships which may be considered as potential competing interests:

One of the authors (Pr. Eric MacDonald) of this article is part of the Editorial Board of the journal. To avoid potential conflicts of interest, the responsibility for the editorial and peer-review process of this article lies with the journal's other editors. Furthermore, the authors of this article were removed from the peer review process and had no, and will not have any access to confidential information related to the editorial process of this article.

Journal Pre-proof